Molecular Understanding of Homogeneous Nucleation of CO2 Hydrates Using Transition Path Sampling

Arjun, A.; Bolhuis, P.G.

DOI
10.1021/acs.jpcb.0c09915

Publication date
2021

Document Version
Final published version

Published in
Journal of Physical Chemistry B

THE JOURNAL OF PHYSICAL CHEMISTRY B
A JOURNAL OF THE AMERICAN CHEMICAL SOCIETY

pubs.acs.org/JPCB

Article

Molecular Understanding of Homogeneous Nucleation of CO_2 Hydrates Using Transition Path Sampling

A. Arjun and P. G. Bolhuis*

Cite This: *J. Phys. Chem. B* 2021, 125, 338–349

Read Online

ACCESS | Metrics & More | Article Recommendations | Supporting Information

ABSTRACT: Carbon dioxide hydrate is a solid built from hydrogen-bond stabilized water cages that encapsulate individual CO_2 molecules. As potential candidates for reducing greenhouse gases, hydrates have attracted attention from both the industry and scientific community. Under high pressure and low temperature, hydrates are formed spontaneously from a mixture of CO_2 and water via nucleation and growth. Yet, for moderate undercooling, i.e., moderate supersaturation, studying hydrate formation with molecular simulations is very challenging due to the high nucleation barriers involved. We investigate the homogeneous nucleation mechanism of CO_2 hydrate as a function of temperature using transition path sampling (TPS), which generates ensembles of unbiased dynamical trajectories across the high barrier between the liquid and solid states. The resulting path ensembles reveal that at high driving force (low temperature), amorphous structures are predominantly formed, with $4^1 5^{10} 6^2$ cages being the most abundant. With increasing temperature, the nucleation mechanism changes, and $5^{12}6^2$ becomes the most abundant cage type, giving rise to the crystalline sI structure. Reaction coordinate analysis can reveal the most important collective variable involved in the mechanism. With increasing temperature, we observe a shift from a single feature (size of the nucleus) to a 2-dimensional (size and cage type) variable as the salient ingredient of the reaction coordinate, and then back to only the nucleus size. This finding is in line with the underlying shift from an amorphous to a crystalline nucleation channel. Modeling such complex phase transformations using transition path sampling gives unbiased insight into the molecular mechanisms toward different polymorphs, and how these are determined by thermodynamics and kinetics. This study will be beneficial for researchers aiming to produce such hydrates with different polymorphic forms.

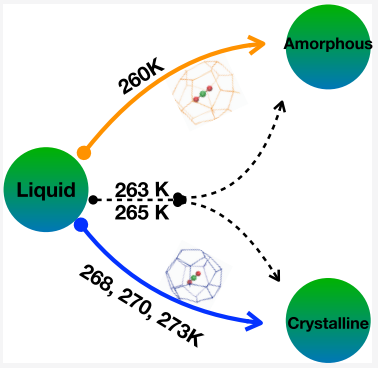

INTRODUCTION

The impact of anthropogenic carbon dioxide on climate is substantial, as evident from the increase in global temperature[1] and associated phenomena. To reduce the effect of the greenhouse gas on global warming, CO_2 capture from the atmosphere is crucial. Hydrate-based gas separation[2] has identified clathrate hydrates as having potential for CO_2 gas storage. One of the technologies aims at storing CO_2 inside water cages in a solid form.[3] Indeed, carbon dioxide molecules can be trapped inside a network of water molecules to form a thermodynamically stable clathrate hydrate. These clathrates are crystalline compounds that have gained significant attention because of their property of storing not only CO_2 but also energy-rich gases, such as CH_4 and H_2. Each of these gases have a socioeconomic factor associated with them. In other applications, CO_2 hydrates are also being considered as fire extinguishers[4] and as refrigerants.[5] The high dissociation enthalpy of CO_2 (500 kJ/kg) compared to that of ice (333 kJ/kg)[6] renders it ideal for cold energy storage applications. Furthermore, there have been reports on extraterrestrial presence of CO_2 hydrates on Mars.[7] Clearly, understanding the formation process of this clathrate is fundamental to the engineering and scientific community. As such, CO_2 hydrates have been studied extensively recently.[8−14]

In contrast to liquid CO_2, which crystallizes into an fcc crystal,[15] a mixture of water and CO_2 gas crystallizes into a thermodynamically stable cubic hydrate clathrate structure under conditions of low temperature and high pressure. The concentration of CO_2 in the clathrate phase is much higher than the solubility of the CO_2 in the liquid mixture. Besides the hydrogen bonds between the ice-like water, the van der Waals interactions between water in the cage lattice, and the guest molecules keep this structure stable. The thermodynamically stable cubic structure 1 (sI) contains small cages built from 20 hydrogen-bonded waters arranged in a pentagonal dodecahedron represented by 5^{12}, where the superscript indicates the 12 faces formed by pentagons. As the 5^{12} building blocks cannot fill space, they are connected by larger cages of 24 waters with 12 pentagonal faces and two hexagonal faces, denoted as $5^{12}6^2$. The ratio of small to large cages is 1:3. Within the cages, small

Received: November 3, 2020
Revised: December 11, 2020
Published: December 31, 2020

https://dx.doi.org/10.1021/acs.jpcb.0c09915
J. Phys. Chem. B 2021, 125, 338−349

guest molecules are encapsulated, with limited translation motion but substantially more rotation and vibration ability. An alternative form of the clathrate structure is sII, which has a different large cage, $5^{12}6^4$, with two more hexagonal faces to relieve the strain. Hydrates can undergo a structural change from sII to sI and other polymorphs,[16] in which arrangements of waters result in different sizes of cavities. In general, sI can contain small (around 0.55 nm) guests, where sII generally occurs with larger (around 0.7 nm) guests. Most research work so far has been done on these two structures. In addition, hydrates can form amorphous structures built from a variety of cage types, including a nonstandard $4^15^{10}6^2$ cage.

The exothermic process of formation of CO_2 hydrates from the dissolved gas mixture in water is a first-order phase transformation, in which a rare random fluctuation in the metastable liquid state creates a "critical" nucleus, which further grows into the stable state. This rare activated process can be interpreted as crossing a high free-energy barrier. With origins in the 1930s, classical nucleation theory (CNT)[17] is the standard framework to explain such activated phase transitions from a liquid to solid state. Computational atomistic modeling of the sI hydrate formation by nucleation has been challenging. This is because the crystallites form nucleates only at moderate driving force, where barriers are high and the transition is an exceedingly rare event. On the other hand, the spatiotemporal resolution for capturing localized fluctuations in the nucleation process is not accessible experimentally, although there have been some efforts in this direction.[18,19]

The majority of the research on hydrates has focused on CH_4 hydrate, which forms the same thermodynamically stable polymorph (sI) with full cage occupancy as CO_2. However, their (metastable) amorphous structures differ, as CO_2 forms nonstandard $4^15^{10}6^2$ cages due to the elongated shape of the guest molecule. Moreover, previous work has indicated that CO_2 reacts differently from CH_4 in hydrate formation.[20] CO_2 has a larger molecular diameter of 5.12 Å, which is larger than methane 4.36 Å. The solubility of CH_4 in water is roughly one in 4000 waters compared to one CO_2 in 1800 waters.[21] A previous study reported that CO_2 is more soluble in water compared to methane[10] because CO_2 has a stronger interaction with water due to a larger dipole moment compared to CH_4, and is henceforth less hydrophobic. This dipole moment destabilizes the large cavity with the Coulombic interactions of the partially negative oxygen molecules of CO_2 and the inward negative field from H_2O, but the short-range interactions between CO_2 and water are still stronger, rendering it as an effective hydrate former.[22] CO_2 has a linear geometry in contrast to the more spherical shape of methane, and a weaker cage guest adsorption interaction compared to methane,[23] indicating that methane stabilizes water cages by adsorption more than carbon dioxide. Indeed, the melting temperature of CO_2 hydrate is typically lower compared to CH_4 as it requires more energy to dissociate the methane hydrate structure.

Recent work[21,24] suggests that the $4^15^{10}6^2$ cage restricts the rotation of the CO_2 molecule in three dimensions and acts as an intermediate metastable cage before transforming into standard 5^{12} and $5^{12}6^2$ cages. The $4^15^{10}6^2$ cage has also been of importance in the formation of ethane clathrate.[25] Metastable intermediates are normally transient and easily transformed in simulations to kinetically and thermodynamically favored stable products but not in clathrates, as this requires substantial hydrogen bond breaking and remaking.

With this background, the need for modeling CO_2 hydrate has been emphasized by the scientific community in the past.[5] Molecular dynamics simulations can provide molecular level understanding of CO_2 hydrate formation. Straightforward MD can access clathrate formation at low temperature or high undercooling. However, at moderate undercooling, the nucleation becomes a rare event, and the high free-energy barrier cannot be easily overcome even when simulating for microseconds.[26,27] That is why previous simulation studies on CO_2 hydrates often focus on high driving force and generate only few reactive trajectories. One way to overcome the rare event problem is using enhanced sampling techniques that change the underlying Hamiltonian of the system (e.g., metadynamics or umbrella sampling), to force the system across the free-energy barrier, at the cost of altering the intrinsic dynamics of the system. Another approach is the use of coarse-grained models that allow faster calculations but may compromise accuracy, dynamics, and molecular details. A third, in principle, exact approach is to sample unbiased dynamical trajectories undergoing the transition between states without prior knowledge of the reaction coordinate. Here, we apply transition path sampling (TPS),[28] which has been used previously to elucidate the molecular mechanism of CH_4 hydrate formation at moderate undercooling.[29] While computationally intensive, TPS yields an ensemble of reactive trajectories that provides statistically significant insights, still exponentially faster than straightforward MD. In addition, TPS allows finding the most salient features of the reaction coordinate. Our TPS simulations and subsequent RC analysis reveal how the mechanism of CO_2 hydrate formation changes when going from high to moderate undercooling. At low temperature, in line with previous straightforward MD studies, amorphous solid hydrates are formed, while at moderate undercooling, the system crystallizes directly into a crystalline sI form. This change in homogeneous nucleation mechanism was seen previously in our work on methane hydrate nucleation and adds a new dimension to understanding the formation of clathrate hydrates.

The paper is organized as follows. In the Methods section, we briefly describe the used techniques and simulation settings. Next, the results are presented and discussed. We end with concluding remarks.

METHODS

Simulation Details. CO_2 and water were described by a modified transferable potentials for the phase equilibria (TraPPE) force field[30] and TIP4P-ice model.[31] A total of 2944 water and 512 CO_2 molecules were used for the simulation in a cubic box with periodic boundary conditions. This system size has been used in previous studies of clathrate nucleation.[29] The modified version of TraPPE has been used previously to study nucleation of CO_2 hydrates.[24,30] The melting temperature for this setting was around 284 K.[30]

All simulations were run using OpenMM 7.1.1.[32] The velocity Verlet with velocity randomization (VVVR) integrator (from openmmtools[33]) was used to integrate the equations of motion. The integration time step was set to 2 fs. Hydrogen bond lengths were constrained. The van der Waals cutoff distance was 1 nm. Long-range interactions were handled by the particle mesh Ewald technique. The MD simulations were performed in the NPT ensemble using the VVVR thermostat (frequency of 1ps) and a Monte Carlo barostat (frequency of 4ps). TPS simulations were performed using the CUDA

https://dx.doi.org/10.1021/acs.jpcb.0c09915
J. Phys. Chem. B 2021, 125, 338−349

platform of OpenMM on a NVIDIA GeForce GTX TITAN 1080Ti GPUs. This is similar to our previous work on methane hydrate. Since the aggregate simulation time is in the order of milliseconds, we choose a low (an order of magnitude smaller than normal) saving frequency for the efficiency of the path sampling and optimizing storage space, which ran into several terabytes.

When simulating in the initial state, the (super)saturated solution is in equilibrium with a spherical bubble of CO_2 gas. A similar bubble gas reservoir setup has been used previously to study methane,[27] ethane,[34] and propane[35] clathrate formation. This spherical bubble reservoir is a consequence of the necessarily small size of the system to make the simulations tractable. The gas bubble has a higher internal pressure than the imposed pressure of 500 bar due to the excess Laplace pressure. From the simulations, we gauge the bubble radius to be of the order of $R \approx 1.5$ nm, leading to a corresponding Laplace pressure of around 1000 bar (see Section 2.8 in the Supporting Information). This higher pressure induces a much stronger driving force than would normally be encountered by increasing the saturation level of the gas.[26] Indeed, the mole fraction of CO_2 in the liquid phase is roughly 0.07−0.08, which, as the solubility of CO2 at these conditions is 0.035,[30] corresponds to a supersaturation of $S \approx 2$. This higher driving force renders the nucleation barrier to be lower but still high enough to avoid spontaneous nucleation (see Section 2.8 in the Supporting Information).

Transition Path Sampling Details. All transition path sampling (TPS) simulations were performed using OpenPathSampling software package.[36] TPS generates unbiased pathways connecting liquid and solid states over a (high) nucleation free-energy barrier. Without a priori requirement of a collective variable describing the reaction coordinate, the transition paths traverse a variety of routes in the rough (free) energy landscape. The reactive paths that are successful in meeting the required conditions constitute an ensemble of trajectories that allow elucidating the mechanism of the process (or reaction) of interest. TPS has been applied before on nucleation Lennard-Jones systems,[37] NaCl,[38] and methane hydrate.[29]

The spring shooting algorithm[39] was used to generate new pathways close to the barrier. The parameters used in spring shooting are stated in Table 1. The initial path was obtained from a brute force molecular dynamics simulation performed at $T = 250$ K and $P = 500$ bar for 1 μs. During the simulation, the system spontaneously solidified (see also Section 1.3.3. in the Supporting Information).

Table 1. Parameters for Spring Shooting and the Source of Initial Paths in TPS Simulation

temperature (K)	spring constant (κ)	frame shift ($\Delta\tau$)	initial path details
260	0.1	100	Brute force (250 K)
263	0.1	100	TPS from 260 K
265	0.1	50 & 100	TPS from 268 & 260 K
268	0.1	200	TPS from 270 K
270	0.1	200	Brute force (250 K)
273	0.1	200	TPS from 270 K

Order Parameter for TPS. TPS samples the landscape connecting the stable states defined by order parameters. In our case, we use the mutually coordinated guest (MCG) order parameter,[40] which counts the number of carbon dioxide molecules involved in the largest solid nucleus in the system. It is a two component order parameter, which uses both CO_2 and water in its calculation. Each CO_2 molecule (guest molecule) is checked for whether its neighboring molecules satisfy a set of geometric constraints.[40] If so, that CO_2 is an MCG monomer. Neighboring MCG monomers are part of the same cluster. The largest connected cluster in the system is then identified using a cluster algorithm. The MCG order parameter is defined as the size of this largest (solid) cluster.

Here, we use MCG-1 (and refer it as MCG) as it checks for any possible occurrence of nucleus formation when compared to MCG-3, which only identifies the stable nucleus.[40] We determined the MCG using a home written code.

Apart from MCG, we evaluated 15 other order parameters, which are all discussed in Section 1.4. in the Supporting Information. These represent nucleus size (calculated in terms of the number of CO_2 and the number of waters in a growing cluster) and nucleus shape (calculated in terms of the number of different cage types, radius of gyration, and F4[41]). These order parameters were used to evaluate the reaction coordinate, as discussed further. All of the order parameters were calculated using the MDTraj python library.[42]

State Definition. The acceptance criterion for TPS requires an order parameter to identify whether the trial trajectory has reached one of the stable states. We use the MCG as an order parameter to determine whether we have reached the liquid or the solid stable state because MCG is more robust than global order parameters, such as F4,[41] and faster to compute compared to full cage analysis. This setup was also successfully applied in our previous work.[29,43] Here, we define the liquid stable state by MCG ≤ 10. We define the solid stable state by the presence of the largest cluster with an MCG of size ≥ 300. An important aspect is that these stable state definitions do not fix the final solid state to be amorphous, crystalline sI, or sII. All structures are acceptable as the final state in the path sampling and the system is free to choose which is more favorable. An amorphous clathrate phase is defined as one in which the $4^1 5^{10} 6^2$ cage type is most abundant, and the cage ratio of $5^{12}6^2$ / $4^1 5^{10} 6^2$ is below unity. This is similar to the more standard cage ratio $5^{12}6^2$ /5^{12}, as used in previous studies.[44,45] The seven fully formed cages (which are 5^{12}, $5^{12}6^2$, $5^{12}6^3$, $5^{12}6^4$, $4^1 5^{10} 6^2$, $4^1 5^{10} 6^3$, and $4^1 5^{10} 6^4$) were evaluated for each reactive trajectory in postanalysis work using CPU cores.

Reaction Coordinate (RC) Analysis. The TPS methodology gives access to the shooting points of each unbiased path that can be used to evaluate the underlying RC. In general, the committor is the optimal RC.[46,47] For any spatial configuration x, the committor $p_B(x)$ is defined as the fraction of trajectories that start at x with Maxwell−Boltzmann-randomized velocities and end in the solid state. Obtaining the exact committor $p_B(x)$ along the reaction pathways is almost unrealistic computationally, and is difficult to interpret. Instead, this high dimensional committor $p_B(x)$ can be approximated by a low dimensional description, which gives insight into the process. We use likelihood maximization (LM)[48] to find the ingredients of the RC for each temperature. Usually, the value of committor is approximately 0 or 1 unless the configuration is close to the dynamical bottleneck of the transition. Since spring shooting focuses shooting points close to the barrier, we get the information about the reaction coordinate at the barrier. The LM method starts with an initial set of candidate order

https://dx.doi.org/10.1021/acs.jpcb.0c09915
J. Phys. Chem. B 2021, 125, 338−349

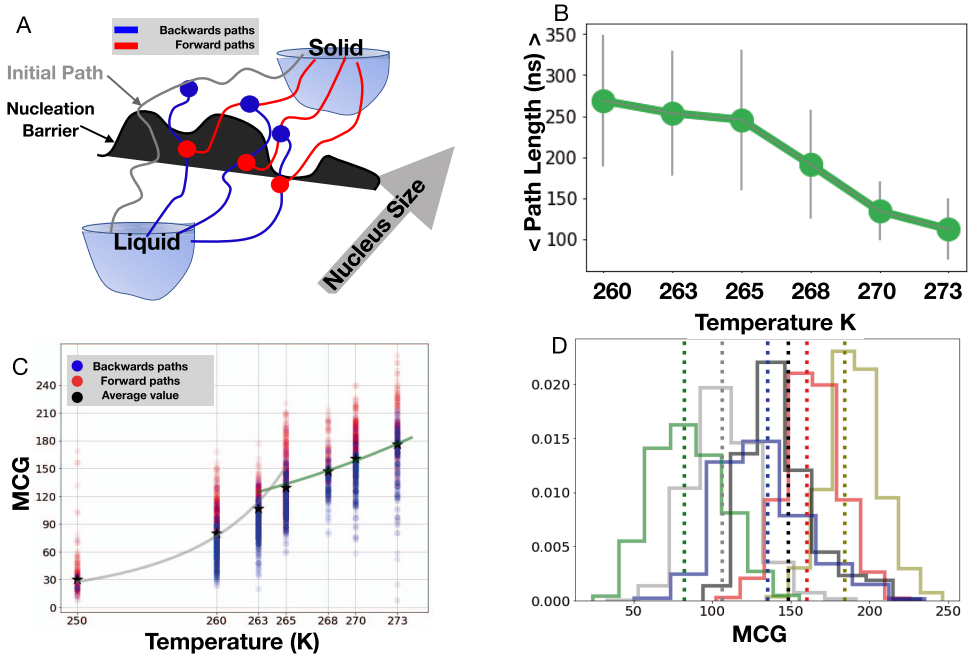

Figure 1. (A) Schematic overview of the one-way shooting method applied on the initial path (gray) that generates forward (red) and backward (blue) paths. The intermediate barrier (shown in black) separates the two states along the size of the growing nucleus (which is an order parameter). (B) Average transition path length from MCG = 10 to 300 as a function of temperature. Each green solid dot represents the ensemble average for a temperature. The gray vertical line at each point shows the spread of path length data for that temperature. The line connecting different temperatures is a guide to the eye. (C) Shooting point locations of the TPS paths that ended in a liquid (blue) or solid (red) state. Black star shows the location of the critical nucleus calculated by averaging forward and backward points. Shooting point data of 250 K is included in this plot, while the TPS details of 250 K are shown in Section 1.3.3 in the Supporting Information. Gray and green curves are a guide to the eye showing the growth in nucleus size with temperature for the amorphous and crystalline channel, respectively. (D) Histograms of the MCG nucleus size in the barrier region (as sampled by the least changed path (LCP)). The location of the critical nucleus from averaging the shooting points is indicated by the dotted line. The green, gray, blue, black, red, and olive curve correspond to 260, 263, 265, 268, 270, and 273 K, respectively.

parameters and finds linear combinations of these OPs with the highest likelihood to reproduce the shooting point data. See the Supporting Information for further details.

RESULTS AND DISCUSSION

Transition Path Sampling. A 1 μs initial straightforward MD trajectory at 250 K, 500 bar exhibited spontaneous nucleation of the solution into an amorphous solid. After an induction time in which transient nuclei appear in the metastable liquid phase, a critical nucleus is formed, which can grow into a full solid. The cage type distribution of this initial path is shown in Figure S2 in the Supporting Information and displays a similar cage population as found before[24] at the same temperature and pressure.

As the barrier increases for higher temperature, straightforward MD is not practical, and we resort to transition path sampling (TPS). Figure 1A depicts the central idea behind the TPS. The spring shooting algorithm performs a Monte Carlo random walk in trajectory space by sampling shooting points close to the transition barrier. Successful partial paths starting from here end up in either the liquid or solid state. The resulting path ensemble was stored for further analysis.

Path ensembles for the transition from a liquid to solid phase were generated at six different temperatures 260, 263, 265, 268, 270, and 273 K. Table 2 shows the statistics of the TPS runs. The quality of sampling the liquid to solid transition paths at a particular temperature can be visualized using path trees, as shown in Figure S5 in the Supporting Information. The fact that paths were sufficiently decorrelated also followed from the fact that CO_2 molecules on average exchanged

Table 2. Spring Shooting Statistics

temperature (K)	trials	acceptance (%)	decorrelated paths
260	564	38	52
263	470	35	49
265	720	32	61
268	214	37	24
270	443	31	45
273	310	32	31

between the liquid and gas reservoir sufficiently regularly. Each transition path exhibits a growing cluster (i.e., nucleus) characterized by CO_2 molecules trapped inside water cages. Analysis of the cage types reveals that at temperature below 265 K, transition paths tend to end in an amorphous solid, while at higher temperature, the paths tend to form sI structures.

The average path length for each temperature is shown in Figure 1B. The duration of paths is Poissonian distributed, as expected (shown in the SI). The average path length clearly increases with decreasing temperature (higher undercooling). This might be caused by the slow dynamics of the molecules (especially water) at lower temperature. Higher undercooling restricts the movement of supercooled water, resulting in a low diffusivity. The transition paths ending in an amorphous solid tend to be longer compared to those leading to a crystal state (shown in Section 2.1 in the Supporting Information). Hence, waters are more kinetically trapped in the amorphous region. For higher crystallinity, we observe shorter transition pathways, corresponding to trajectories that commit faster to the final

https://dx.doi.org/10.1021/acs.jpcb.0c09915
J. Phys. Chem. B 2021, 125, 338−349

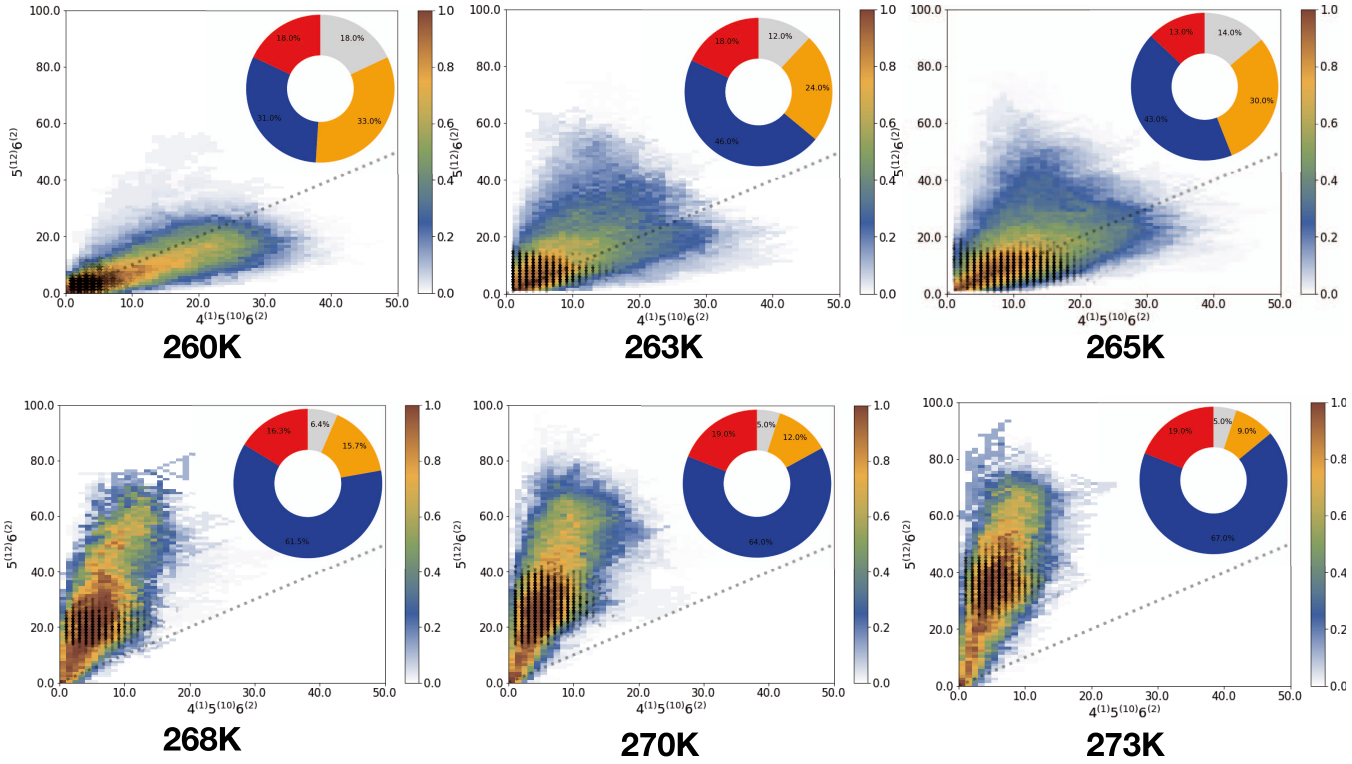

Figure 2. Path densities from TPS for different temperatures as a function of $4^1 5^{10} 6^2$ (x axis) and $5^{12} 6^2$ (y axis) cage. The dotted line in each plot is the 1:1 reference line: a guide to the eye, separating amorphous and crystalline domains. The black dots overlaying the path density plot are the scatter plots of the least changed path (LCP), indicating the barrier region. The circle diagrams show the overall cage fractions in the LCP, with the red color representing 5^{12} cages, blue $5^{12} 6^2$ cages, orange $4^1 5^{10} 6^2$ cages, and the gray color indicating the percentage of $5^{12} 6^3$, $5^{12} 6^4$, $4^1 5^{10} 6^3$, and $4^1 5^{10} 6^4$ cages together.

state (see Figure 1B). On the other hand, at moderate undercooling, the pathways follow the crystalline channel and reach the intermediate or crystalline domain relatively quickly. In the following sections, we analyze this behavior in more detail.

Effect of Finite System Size. In the Methods section, we already alluded to the consequence of the finite system size. The spherical gas reservoir has a radius of roughly 1.5 nm, which leads to a Laplace pressure of about 1000 bar. The total pressure of 150 MPa in the gas reservoir induces a higher saturation in the liquid phase, which, in turn, influences the driving force $\Delta\mu$. The higher driving force will lower the homogeneous nucleation barrier compared to the situation without a curved interface. However, the barrier will still be substantially high so that the nucleation event is rare (see the Supporting Information for a numerical treatment).

During a TPS trajectory undergoing the nucleation event, the CO_2 molecules that form the growing nucleus will be transported from the supersaturated liquid, thus lowering the concentration of dissolved carbon dioxide molecules. To replenish these molecules, CO_2 from the reservoir is dissolved in the liquid, effectively transporting CO_2 from the gas to the crystal. This means that the gas reservoir shrinks during the homogeneous nucleation process while the crystal nucleus grows. This changing reservoir size might, in turn, again lead to an increase in Laplace pressure and driving force. In the SI, we show that this change is modest, and that (at least for the lower temperature) until the postcritical regime is reached, the radius of the spherical reservoir, as well as the pressure, hardly changes. In fact, the concentration of dissolved carbon dioxide seems to slightly decrease. Of course, in the very late postcritical stages of the nucleation process, this will change, and there, the driving forces will be larger.

At higher temperatures, the critical nucleus can also become so large that it will be influenced by its periodic image. However, this is not the case for critical nuclei below MCG = 150, corresponding to temperatures below 268 K.

Nucleation Mechanism for Different Temperatures. The solid nucleus is formed in the bulk of the liquid phase, and is, while growing, always wetted by a liquid layer of water molecules. Initially, the cluster is composed of partially formed cages, which, as the nucleus grows, transform into fully formed cages. The number of fully formed cages remains significantly lower than the MCG value, indicating that many guest molecules belonging to the cluster have a partially formed cage. A previous study[24] suggested that the first fully formed cage is of the $4^1 5^{10} 6^2$ type. While we also observe this at the lower temperatures of 260 and 263 K, for higher temperatures, e.g., 270 and 273 K, the first formed cage is either 5^{12} or $5^{12} 6^2$, indicating a significant qualitative change in the mechanism. There are many short-lived fluctuating cages that form and dissolve again. This can be observed in the videos in the Supporting Information.

Figure 2 visualizes the path ensembles as path densities in the plane of the number of $5^{12} 6^2$ cages and the number of $4^1 5^{10} 6^2$ cages. The path density is high in the origin, corresponding to the initial liquid solution phase without any clusters, and extends into the plane at a certain slope. This slope becomes larger with increasing temperature, as the population of $5^{12} 6^2$ increases, indicating an increase of the cage ratio $5^{12} 6^2 / 4^{10} 5^{12} 6^2$. Also, other cage ratios increase notably, in particular, the $5^{12} 6^2 / 5^{12}$ ratio; also see Figure 8 below. This

https://dx.doi.org/10.1021/acs.jpcb.0c09915
J. Phys. Chem. B 2021, 125, 338−349

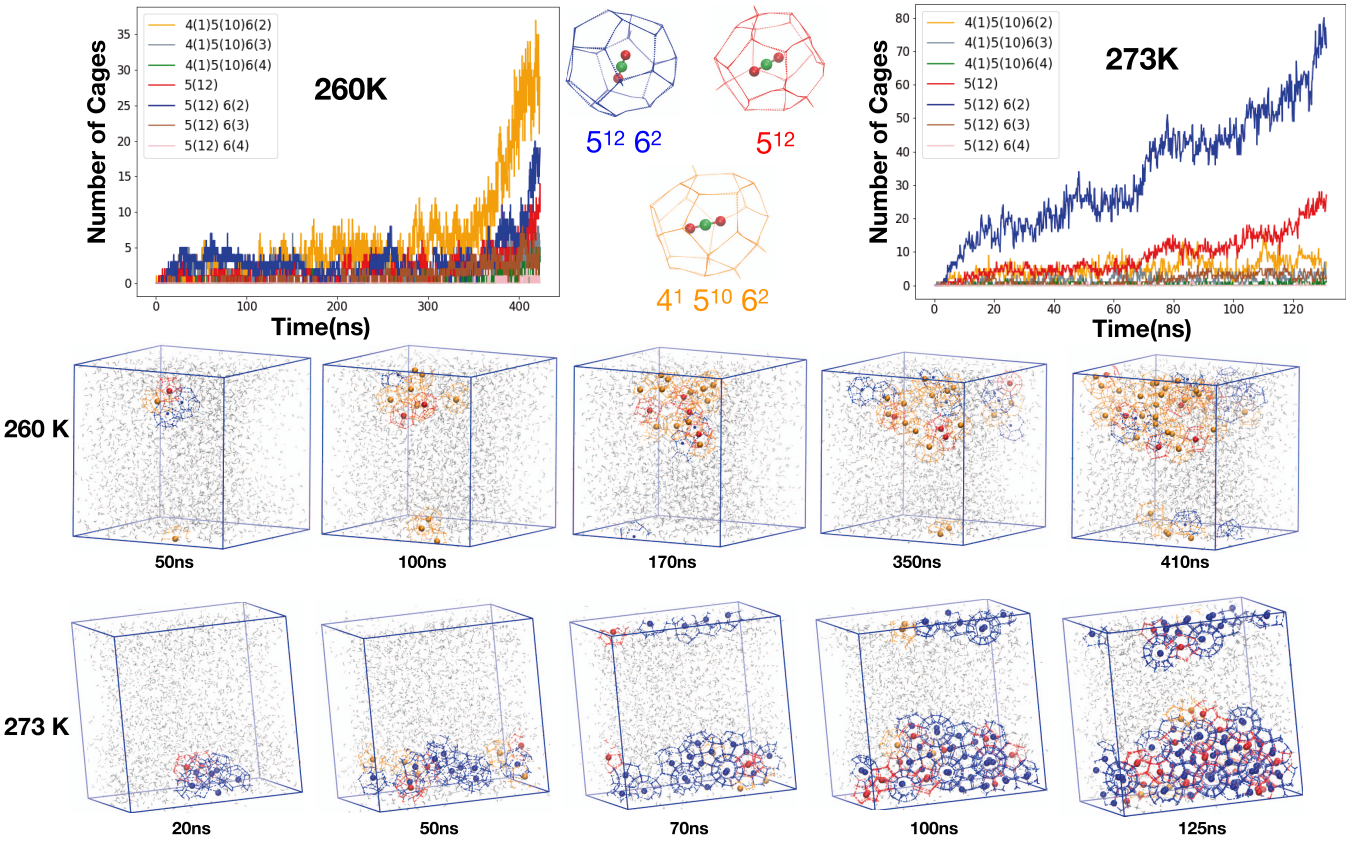

Figure 3. Top: evolution of different cage types in a nucleation trajectory for two temperatures. The three main cage types, namely, $5^{12}6^2$ (blue), 5^{12} (red), and $4^15^{10}6^2$ (orange) showing a trapped CO_2 molecule at the top. The hydrogen bonds are indicated by thin lines connecting the oxygen atoms of the waters at the vertices. Bottom rows: simulation snapshots taken along these trajectories showing the emergence of cage structures. The gray lines represent unstructured waters in the background. The CO_2 molecules outside the cage structures are not shown for clarity.

gradual increase corresponds to a shift from the amorphous to the crystalline mechanism. The formation of the $5^{12}6^2$ cage type is associated with increasing crystallinity of the hydrate, whereas the formation of $4^15^{10}6^2$ or 5^{12} cage type is characteristic of amorphous of hydrates. The switch between the mechanism or 'channels' can be observed in the path density in the $4^15^{10}6^2$–5^{12} plane (see Section 2.4 in the Supporting Information for analysis). The crystalline solid tends to form more 5^{12} cages because it can associate with $5^{12}6^2$ cages to form an sI structure. Note that switching is not as easy as in the case of methane hydrate. This can point at a higher barrier between the two channels, which, in turn, might be caused by the larger qualitative difference between the amorphous and sI structures for CO_2.

Figure 3 shows the evolution of the cage type composition of a typical individual path in the amorphous and crystalline channels. For the path ending in an amorphous solid at 260 K, the growing nucleus is predominantly composed of the $4^15^{10}6^2$ cage type, which in the end is roughly two times more abundant than any other cage type. At 50 ns, the nucleus consists of a mixture of various half-formed cages (that encapsulate the MCG monomers) with already several $4^15^{10}6^2$, $5^{12}6^2$, and 5^{12} fully formed cages present. At 100 and 170 ns into the trajectory, the population of $4^15^{10}6^2$ cages increase, while the $5^{12}6^2$ cage type becomes less abundant. In between 350 and 400 ns, all of the fully formed cages start to increase in number, which indicates that the growth regime in the nucleation process has been reached. At the end, the nucleus firmly has an amorphous structure. In contrast, the growing nucleus in the trajectory for 273 K mostly consists of $5^{12}6^2$ cages from the very beginning. At 20 ns, the $5^{12}6^2$ cage type is about five times more prevalent compared to the other cage types. As time progresses, at 50, 70, and 100 ns, the population of $5^{12}6^2$ cage type increases consistently, while the other cage types mostly stay low in number and constant. In the final frame at 125 ns, the crystalline sI solid spans the simulation box and has a cage ratio $5^{12}6^2/\ 5^{12} \approx 3$. This is also clearly visible in the sequence of simulation boxes along the nucleation pathway in the lower panels of figure Figure 3. Since nucleation is a stochastic process, the formation of the initial cages varies in each trajectory at each temperature.

Critical Nucleus Region. As the spring shooting algorithms keeps the shooting points close to the barrier, the distribution of these points by necessity is a proxy for the critical region. We can use the nucleus size, as measured by MCG, for each shooting point to estimate the critical nucleus size. In Figure 1C, we plot the shooting point locations, where the blue points lead to the liquid state and the red points to the solid state. The average is indicated by a black dot (the median gives similar results).

Another related way to identify the critical region or the location of the nucleation barrier is via the so-called least changed path (LCP), which demarcates the barrier (see SI). It diffuses around the barrier region bounded by the forward and backward shooting points at each side of the nucleation barrier. Figure 1D gives the MCG distribution in the sampled region based on LCP. The location of the critical nucleus (average of

https://dx.doi.org/10.1021/acs.jpcb.0c09915
J. Phys. Chem. B 2021, 125, 338−349

shooting points) is plotted in dotted lines. Both measures of the critical nucleus size give similar results.

Clearly, the nucleus size increases with temperature, as expected from CNT (see Section 2.2 in the Supporting Information for analysis). At the temperatures around 263−265, there seems to be a change in the trend, indicating a change in the mechanism. CNT predicts the critical nucleus size to grow as $r = 2\gamma/\rho\Delta\mu$. Assuming a constant surface tension γ and that the driving force changes linearly with temperature, this leads to a temperature dependence for the critical nucleus size $n \sim 1/(a + bT)^3$. We fitted the observed critical nucleus sizes below and above 264 K to these nonlinear equations, and included the fitted curves in Figure 1 as a guide to the eye.

The circular diagrams in Figure 2 show the cage type composition of the nucleus at the top of the barrier, as calculated from the LCP. Clearly, the composition in the critical region becomes more crystalline with lower undercooling. The cage composition shows a shift from an amorphous to a crystalline sI-type barrier region. At 260 K (also at 250 K; included in Section 1.3.3 in the Supporting Information), the barrier is mostly dominated by $4^1 5^{10} 6^2$ cages, indicating an amorphous cluster. There is a gradual shift to the $5^{12}6^2$ cage at 263 and 265 K. Beyond this, 268, 270, and 273 K all report $5^{12}6^2$ cage type being the most dominant one, typical for sI crystals. We stress that at 263 and 265 K, both channels are accessible and switching is possible (see Section 2.3 in the Supporting Information).

Cage Type Composition of the Nucleus. The characteristic features of solid hydrates are encoded in the cage types that entrap the guest molecule. We identified seven main types of fully formed cages, which we use to follow how the nucleation process evolves. Focusing first at the start of the nucleation process, we measured the fully formed cages in the initial 8 ns of each trajectory in the entire path ensemble for each temperature, shown as bar graphs in Figure 4A. With increasing temperature, the $5^{12}6^2$ cage type clearly starts to dominate (e.g., for 273 K). In contrast, the $4^1 5^{10} 6^2$ cage type is only most abundant for lower temperatures (e.g., for 260 K). This result is independent of the interval, as similar results are obtained for first 2 and 4 ns (see in Section 2.5 in the Supporting Information).

Second, we extract cage type information from the LCP, which corresponds to the top of the barrier region. In line with the first formed cages, shown as bar graphs in Figure 4B. the barrier region is also dominated by the $5^{12}6^2$ type for 268, 270, and 273 K.

Third, we identified the fully formed cage types for frames in which a trajectory reaches the solid state, i.e., MCG = 300. This distribution is shown in Figure 4C, as bar graphs and scatter plots in Figure 5, where each point is a single frame. Interestingly, the total number of fully formed standard cages increases with increasing crystallinity, i.e., with increasing temperature. The same increasing trend is followed by the $5^{12}6^2$ and 5^{12} cage types, but, in contrast, an opposite trend is followed for the $4^1 5^{10} 6^2$ cage type. The lower temperature path ensembles show a higher number of $4^1 5^{10} 6^2$ cage type, which characterizes the amorphous nature of the solid hydrate. Note that the total number of fully formed cages is smaller than MCG = 300, indicating that the surface of the nucleus contains many partially formed cages.

The increase in the total number of fully formed cages with increasing temperature has been seen before for methane hydrate nucleation.[49] The relative increase in nucleus size along the nucleation process can also be seen (for any specific temperature) in Figure 4A−C, which, respectively, correspond to the precritical, critical, and postcritical nucleus.

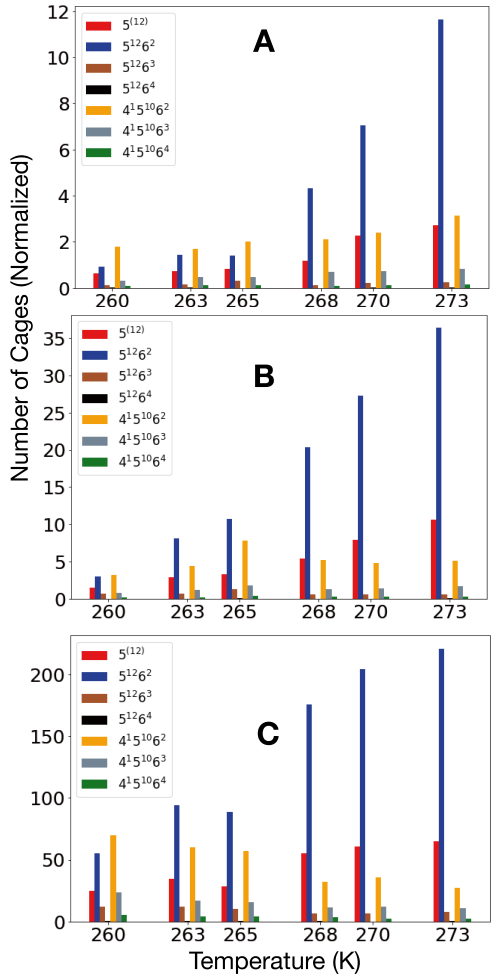

Figure 4. Average number of fully formed cages of a certain type per nucleus formed at different stages along the nucleation process for each temperature. (A) First 8 ns of the entire path ensemble. (B) LCP. (C) Last frame of each trajectory. The sum of the bars for a particular temperature is the total amount of seven fully formed cages. Note that the number of cage increases with temperature.

Unlike methane hydrate nucleation, where we observed some trajectories nucleating into a sII hydrate (Figure S4 in[29]), none of the trajectories of the CO_2 hydrate nucleation formed a $5^{12}6^4$ and 5^{12} cage-rich sII structure at the simulated conditions. Hence, the bar corresponding to $5^{12}6^4$ cage is almost negligible.

Growth Rate of Nucleus. Besides structural information, we can also extract kinetic (time-dependent) information about the nucleation of CO_2 hydrate, in particular, the growth rate. The growth of the nucleus size can be measured in terms of MCG per unit time. To compute this rate, the transition paths in the ensemble are divided into equidistant windows of 30 MCG units between 0 and 300. For each of these windows, we measure an average time taken by transition paths to enter and leave the window (without any recrossing), i.e., the mean first passage time. The inverse of this average first passage time gives the rate of growth of MCG units for each window, which is plotted for various temperatures in Figure 6.

https://dx.doi.org/10.1021/acs.jpcb.0c09915
J. Phys. Chem. B 2021, 125, 338−349

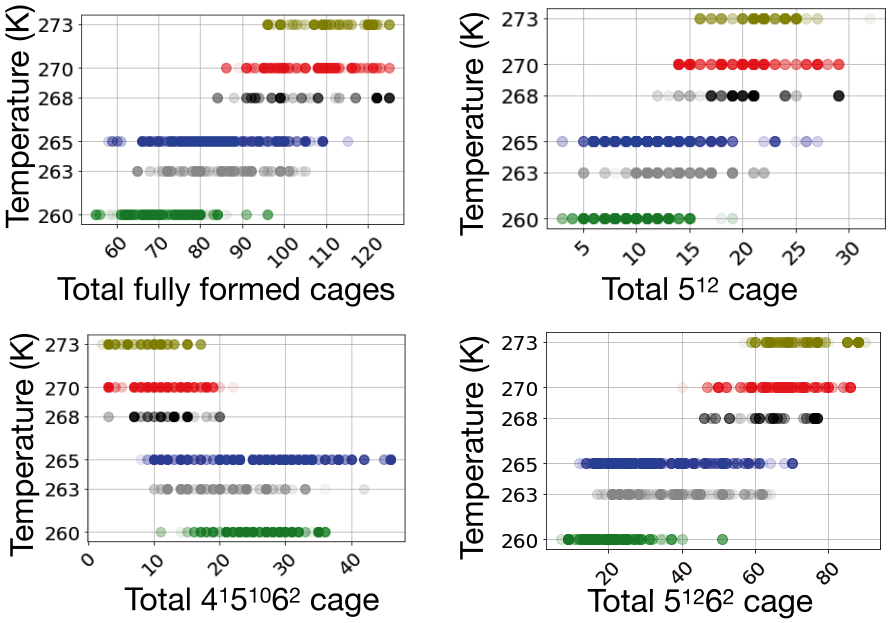

Figure 5. Scatter plots showing the type of cages formed in the last frame (solid state of TPS) of each reactive path in TPS. While the total number of fully formed cages, $5^{12}6^2$ and 5^{12} cages increase with temperature, $4^15^{10}6^2$ cage population decreases with increasing temperature, which corresponds to increasing crystallinity of CO_2 hydrates.

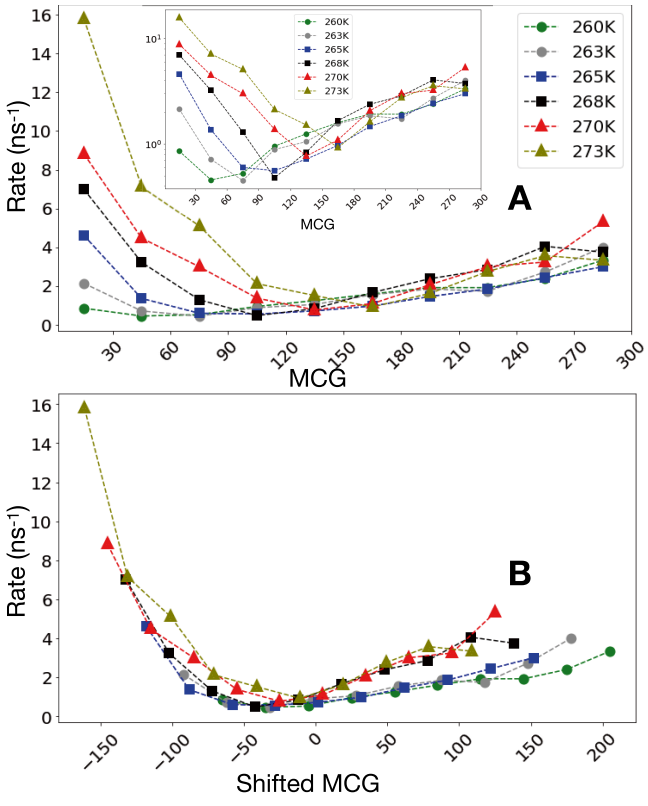

Figure 6. (A) Growth of the MCG calculated in a window of 30 MCG. The inset shows the same plot in the log scale. (B) Data from the above plot is shifted based on each temperature's critical nucleus size such that each point shows the distance from the critical nucleus. The green, gray, blue, black, red, and olive curves are for 260, 263, 265, 268, 270, and 273 K, respectively.

Clearly the growth rate starts for small nuclei between 1 MCG/ns for the lowest and 10 MCG/ns for the highest temperature, and then decreases with MCG. For all temperatures, the minimal growth rate of around 0.5 MCG/ns is reached at the top of the barrier (i.e., the critical nucleus), after which the rate increases again. As the free energy is flat at the top of the barrier, the system behaves diffusively there. Away from the top, the drift caused by the gradient of the free energy becomes substantial, leading to a larger growth rate. This behavior was also observed for methane hydrate.[29]

The location of the lowest growth rate increases with temperature and is in line with the shooting point analysis and LCP, as shown in Figure 1D. The growth rate in Figure 6A for each temperature differs in the precritical region but is remarkably similar in the postcritical region. This similar behavior is even starker in the bottom panel of Figure 6, which shows the growth rate as a function of the MCG, shifted relative to the critical nucleus size. Here, the precritical region also shows roughly the same growth rate for all temperatures. In the postcritical region, the curves split into two sets, one with a higher rate (268, 270, 273 K) and with a lower growth rate (260, 263, 265 K). The high-temperature growth is around twice as high as the low temperature. This matches the fact that amorphous paths take more time to nucleate compared to crystalline paths.

Reaction Coordinate Analysis. We apply likelihood maximization on the set of the shooting points to find the best low dimensional reaction coordinate (RC). The complete set of order parameters and shooting points used to evaluate the RC are discussed in the Supporting Information. The order parameters considered include the size of the growing solid nucleus in terms of CO_2 molecules, and water molecules with the different cage types involved. We also consider local and global geometry in terms of the radius of gyration and the F_4 value. For a full list, see Section 1.4 in the Supporting Information.

For 260 K (and, in fact also, for 250 K), the reaction coordinate is determined by only a single collective variable (either MCG or the number of waters in the nucleus), the size of the nucleus. This is in line with our previous result on

https://dx.doi.org/10.1021/acs.jpcb.0c09915
J. Phys. Chem. B 2021, 125, 338−349

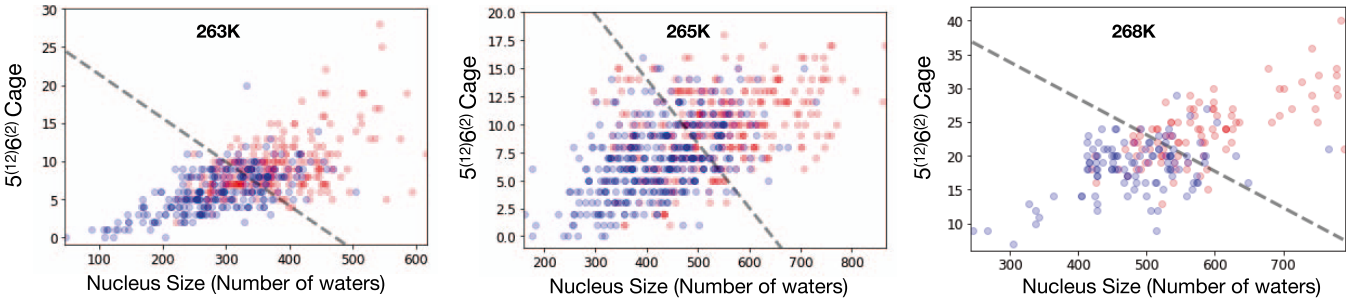

Figure 7. Predicted dividing surface (p_B = 0.5) along the reaction coordinate (dotted black line) shown for 263, 265, and 268 K. The blue and red dots show each forward and backward shooting points from the respective TPS ensemble. The equation for these lines and other ranked reaction coordinates are shown in Section 2.7 in the Supporting Information.

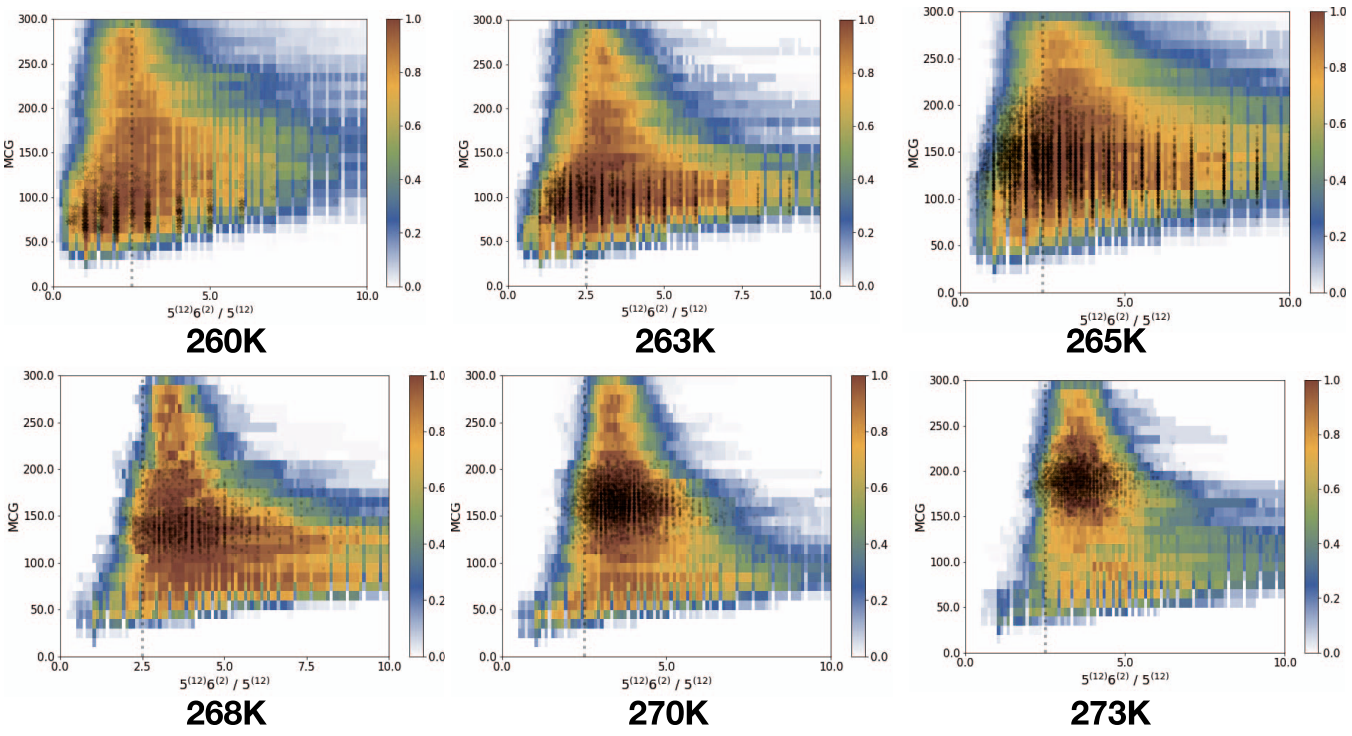

Figure 8. Path densities from TPS for different temperatures as a function of the MCG vs $5^{12}6^2/5^{12}$ cage ratio. The dotted line is a guide to the eye plotted at $5^{12}6^2/5^{12}$ = 2.5. Note that this line is not able to distinguish the amorphous vs crystalline (as done for $5^{12}6^2/5^{12}$ = 1.0 in Figure 2 of our ref29).

methane hydrates,[29] for which we showed that at high undercooling, where amorphous solid nucleates, the most important degree of freedom comprises just the size of the growing nucleus. For 263, 265, and 268 K, the reaction coordinate is two dimensional in nature and composed of size of the nucleus and the crystallinity, as measured by the $5^{12}6^2$ large cage content. This is also analogous to the sampling of 280 and 285 K for methane hydrate,[29] where the structural signature for a growing crystalline nucleus becomes important apart from the size of the nucleus. This two-dimensional reaction coordinate is shown in Figure 7, where each dot represents a TPS trial and the color corresponds to the state reached from that trial. Interestingly, the reaction coordinate shifts back to being one dimensional at 270 and 273 K. The primary reason for this shift is because the nucleus already contains fully formed cages that are in sI geometry and stable (implying that they do not dissociate like half-formed surface cages). Hence, the growing nucleus has already attained its stable polymorphic form in which the cage ratio does not change any longer, and thus the key ingredient to describe the growth is again only the nucleus size. This variation can be visualized in Figure 8, where the location of the critical nucleus is indicated by the shooting points (black dots) on top of the path density. The x axis of these path densities indicates the $5^{12}6^2/5^{12}$ cage ratio, which is the main cage type in crystalline sI hydrate.

Comparing CO_2 with CH_4 Hydrate Nucleation. For both CO_2 and CH_4 hydrates, the sI structure is the thermodynamically stable polymorph. However, their respective nucleation mechanisms seem to differ. We have shown previously that at a pressure of P = 500 bar, a CH_4−water solution forms an amorphous hydrate for temperature below 280 K, and forms an sI solid for higher temperature. Here, we find that CO_2−water mixture tends to form sI hydrate at a temperature above 263−265 K.

At 270 K (where both CO_2 and CH_4's TPS data can be directly compared), the CO_2 system nucleates into an sI crystal, while the CH_4 system forms an amorphous solid. This

https://dx.doi.org/10.1021/acs.jpcb.0c09915
J. Phys. Chem. B 2021, 125, 338−349

is most likely related to the lower melting point of 284 K[30] for a CO_2 hydrate, which means the degree of undercooling is much lower for CO_2 than for CH_4 (which has a melting temperature of 302 K). When looking at the same degree of undercooling, we should compare the TPS simulation of CH_4 at the 280 K case, with the TPS simulation of CO_2 at the 263 K case. Indeed, in both cases, the switch from amorphous to crystalline phase occurs at these temperatures.

The two hydrates clearly differ in the structure of the amorphous solid. While the $4^15^{10}6^2$ cage hardly plays a role for CH_4 hydrates, it is important for CO_2, which, due to its linear geometry, fits well inside an elliptical cage. Moreover, the first formed cage in the amorphous paths is $4^15^{10}6^2$ in CO_2 hydrates while 5^{12} in methane hydrate. For both hydrates, the $5^{12}6^2$ cage type forms first in the crystalline paths.

Another difference is that at 270 K, the CO_2 paths have an average length of 134 ns compared to 408 ns for CH_4 (shown in Figure 1C of ref29) at the same temperature. This can be explained by a higher growth rate of the CO_2 nucleus compared to the CH_4 case (and has been seen even experimentally[50]), which, in turn, is caused by the higher solubility of CO_2 in water. As more number of CO_2 molecules dissolve in water compared to CH_4 in water, the growth is also higher. Comparing individual trajectories between the CO_2 and CH_4 cases shows that there are more fluctuations in the growing nucleus in the case of CO_2 hydrate, owing to its less suitable shape as well as the higher solubility.

We provide a rough estimate of the barrier height based on CNT in Section 2.8 in the Supporting Information. The free-energy barrier to nucleation is about 65 kT for T = 260 K, 80 kT for 265 K and 100 kT for 270 K. This is in line with our previous work on methane hydrates.

CONCLUSIONS

In this work, we performed extensive path sampling simulations (exceeding 1.3 ms simulation time) of the homogeneous nucleation of solid hydrate in a CO_2−water mixture at high pressure (500 bar) and moderate undercooling. The path ensembles gave detailed atomistic insight into the mechanism of the nucleation process. The main conclusion is that with increasing temperature—lower driving force—the nucleation mechanism switches from forming a metastable amorphous phase to nucleating directly into the stable crystalline sI polymorphs.

At temperatures below 265 K, the amorphous solid CO_2 hydrates tend to be formed with a high fraction of the $4^15^{10}6^2$ cage type, while for temperatures above 265 K, the $5^{12}6^2$ cage population increases, leading to the formation of the sI polymorph. Figure 9 schematically depicts the overall nucleation mechanism.

This switching behavior is very similar to that observed for methane hydrate,[29] albeit occurring at a lower temperature of 263−265 K instead of 280 K, most likely due to the difference in melting temperature between the two hydrates. Also, the precise mechanics details differ; the amorphous channel in CO_2 hydrate is dominated by the $4^15^{10}6^2$ cage type, whereas for CH_4, the amorphous channel is dominated by 5^{12} cages (the methane hydrate data are shown in Section 2.6 in the Supporting Information).

In the last decades, several explanations and interpretations have been put forward about the mechanism of homogeneous CO_2 hydrate nucleation. Using Monte Carlo simulations and umbrella sampling (at 220 K and 4 MPa), Radhakrishnan and

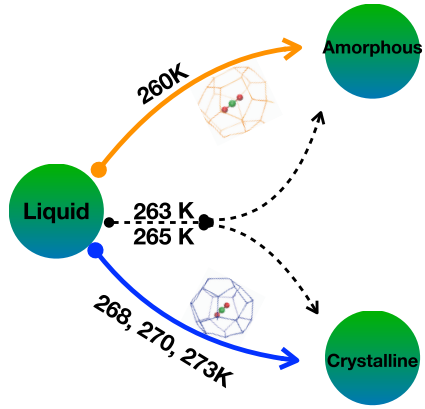

Figure 9. Overall scheme of nucleation is shown in this schematic picture. The amorphous channel is shown to exist for the temperature at 260 K and lower temperatures (based on TPS at 250 K shown in Section 1.3.3 in the Supporting Information). At 263 and 265 K, both crystalline and amorphous channels are accessible. For temperatures higher than 268 K, only the crystalline channel is accessible. The water cages shown in orange and blue indicate $4^15^{10}6^2$ and $5^{12}6^2$ cages, respectively, showing the predominant cage type.

Trout[51] suggested the local structuring hypothesis stating that the guest molecules first order themselves in this formation process, followed by the arrangement of waters around them. This hypothesis countered the previous labile cluster mechanism of Sloan,[52] stating that nucleation is initiated by polyhedral cages of water forming around the guest molecules, which later associate together into a solid nucleus. The blob hypothesis[53] combined these two concepts and suggested an intermediate metastable amorphous phase before the formation of a thermodynamically stable polymorph, where the amorphous solid consists of a noncrystalline "blob" of guest molecules and waters. This amorphous solid in the case of CO_2 hydrate was proposed to be abundant in the $4^15^{10}6^2$ cage.[21,24] In this work, we found that this hypothesis is only valid for higher undercooling. With increasing temperature, the sI forming cages, namely, $5^{12}6^2$ and 5^{12}, start to become more abundant. We note that this notion is against the Ostwalds step rule, which postulates that the nucleation process first enters a metastable phase before the final stable state is formed.

In addition to the mechanism, we studied various other properties of the nucleating solids, such as the critical nucleus size, composition, and shape, as well as kinetics of growth and the reaction coordinate are computed from the extensive simulation data.

The critical nucleus was found to increase with temperature and behave qualitatively in line with the predictions from CNT. The composition of the critical nucleus changed with increasing temperature from being dominated by $4^15^{10}6^2$ cages to mostly dominated by $5^{12}6^2$, in line with the mechanism. Just as in the case of methane, the critical nucleus already has the structural signature of the final phase.

The growth rate of the nucleus size is largest for precritical nuclei and minimal for critical nuclei. The precritical rate increases with the distance from the critical nucleus, which can become larger for higher temperature. Also, the diffusivity increases with temperature, leading to an increased growth rate.

Finally, we performed reaction coordinate analysis based on the set of shooting points. Interestingly, the optimal reaction coordinate switches from a 1D to a 2D model and back to a

https://dx.doi.org/10.1021/acs.jpcb.0c09915
J. Phys. Chem. B 2021, 125, 338−349

single variable again with decreasing nucleation driving force, i.e., increasing temperature. To the best of our knowledge, this is the first time that such a reaction coordinate is being reported for hydrate nucleation.

We stress that our simulations are influenced by the finite size of the system. In particular, the small spherical gas reservoir causes a large Laplace pressure, and thus a larger driving force. While this reduces the effective homogeneous nucleation barriers, these barriers are still substantial, requiring rare event techniques such as TPS. Notwithstanding these caveats, we believe that the predicted mechanistic results are qualitatively also valid at lower driving forces.

This study on homogeneous nucleation on CO_2 hydrate will benefit both scientific and industrial researchers. For instance, understanding how polymorph selection is achieved can potentially help synthetic production of these hydrates. Since the hydrate homogeneous nucleation rate is strongly dependent on thermodynamic conditions, a natural extension of this project will be to estimate the nucleation rate using TIS for amorphous and crystalline channels.

■ ASSOCIATED CONTENT

Supporting Information

The Supporting Information is available free of charge at https://pubs.acs.org/doi/10.1021/acs.jpcb.0c09915.

Transition from the liquid phase to thesolid phase at at 260 and 273 K for CO_2 hydrate formation. We also provide videos that illustrate the switching of pathways when projected on two dimensional path density plot (ZIP)

Materials and methods; system setup; order parameters; transition path sampling setup and details; reaction coordinate analysis by likelihood maximization (LM); results; effects of the small system size; driving force during nucleation (PDF)

■ AUTHOR INFORMATION

Corresponding Author

P. G. Bolhuis − *van 't Hoff Institute for Molecular Sciences, University of Amsterdam, 1090 GD Amsterdam, The Netherlands;* orcid.org/0000-0002-3698-9258; Email: p.g.bolhuis@uva.nl

Author

A. Arjun − *van 't Hoff Institute for Molecular Sciences, University of Amsterdam, 1090 GD Amsterdam, The Netherlands;* orcid.org/0000-0002-6831-6621

Complete contact information is available at: https://pubs.acs.org/10.1021/acs.jpcb.0c09915

Notes

The authors declare no competing financial interest.

■ ACKNOWLEDGMENTS

A.A. and P.G.B. acknowledge funding from the Industrial Partnership Programme 'Computational Sciences for Energy Research' (Grant No. 15CSER051) of the Foundation for Fundamental Research on Matter (FOM), which is a part of the Netherlands Organization for Scientific Research (NWO). This research program is cofinanced by Shell Global Solutions International B.V. We acknowledge support from the Nederlandse Organisatie voor Wetenschappelijk Onderzoek (NWO) for the use of supercomputer facilities.

■ REFERENCES

(1) Solomon, S.; Plattner, G.-K.; Knutti, R.; Friedlingstein, P. Irreversible climate change due to carbon dioxide emissions. *Proc. Natl. Acad. Sci. U.S.A.* **2009**, *106*, 1704−1709.

(2) Xu, C.-G.; Li, X.-S.; Lv, Q.-N.; Chen, Z.-Y.; Cai, J. Hydrate-based CO2 (carbon dioxide) capture from IGCC (integrated gasification combined cycle) synthesis gas using bubble method with a set of visual equipment. *Energy* **2012**, *44*, 358−366.

(3) Li, X.-S.; Xia, Z.-M.; Chen, Z.-Y.; Yan, K.-F.; Li, G.; Wu, H.-J. Gas hydrate formation process for capture of carbon dioxide from fuel gas mixture. *Ind. Eng. Chem. Res.* **2010**, *49*, 11614−11619.

(4) Hatakeyama, T.; Aida, E.; Yokomori, T.; Ohmura, R.; Ueda, T. Fire extinction using carbon dioxide hydrate. *Ind. Eng. Chem. Res.* **2009**, *48*, 4083−4087.

(5) Sun, Q.; Kang, Y. T. Review on CO2 hydrate formation/dissociation and its cold energy application. *Renewable Sustainable Energy Rev.* **2016**, *62*, 478−494.

(6) Marinhas, S.; Delahaye, A.; Fournaison, L.; Dalmazzone, D.; Fürst, W.; Petitet, J.-P. Modelling of the available latent heat of a CO2 hydrate slurry in an experimental loop applied to secondary refrigeration. *Chem. Eng. Process.: Process Intensif.* **2006**, *45*, 184−192.

(7) Milton, D. J. *Carbon dioxide hydrate and floods on Mars*, 1974.

(8) Dashti, H.; Thomas, D.; Amiri, A.; Lou, X. *Computer Aided Chemical Engineering*; Elsevier: 2019; Vol. *46*, pp 1687−1692.

(9) Falenty, A.; Qin, J.; Salamatin, A.; Yang, L.; Kuhs, W. Fluid composition and kinetics of the in situ replacement in CH4-CO2 hydrate system. *J. Phys. Chem. C* **2016**, *120*, 27159−27172.

(10) He, Z.; Gupta, K. M.; Linga, P.; Jiang, J. Molecular insights into the nucleation and growth of CH4 and CO2 mixed hydrates from microsecond simulations. *J. Phys. Chem. C* **2016**, *120*, 25225−25236.

(11) Li, Q.; Fan, S.; Chen, Q.; Yang, G.; Chen, Y.; Li, L.; Li, G. Experimental and process simulation of hydrate-based CO2 capture from biogas. *J. Nat. Gas Sci. Eng.* **2019**, *72*, No. 103008.

(12) Babu, P.; Linga, P.; Kumar, R.; Englezos, P. A review of the hydrate based gas separation (HBGS) process for carbon dioxide pre-combustion capture. *Energy* **2015**, *85*, 261−279.

(13) Bai, D.; Chen, G.; Zhang, X.; Wang, W. Microsecond molecular dynamics simulations of the kinetic pathways of gas hydrate formation from solid surfaces. *Langmuir* **2011**, *27*, 5961−5967.

(14) Bai, D.; Chen, G.; Zhang, X.; Sum, A. K.; Wang, W. How properties of solid surfaces modulate the nucleation of gas hydrate. *Sci. Rep.* **2015**, *5*, 1−12.

(15) Svishchev, I. M.; Kusalik, P. G. Crystallization of molecular liquids in computer simulations: Carbon dioxide. *Phys. Rev. Lett.* **1995**, *75*, 3289.

(16) Schicks, J. M.; Ripmeester, J. A. The coexistence of two different methane hydrate phases under moderate pressure and temperature conditions: Kinetic versus thermodynamic products. *Angew. Chem., Int. Ed.* **2004**, *43*, 3310−3313.

(17) Volmer, M.; Weber, A. Keimbildung in übersättigten Gebilden. *Z. Phys. Chem.* **1926**, *119*, 277−301.

(18) Plemmons, D. A.; Suri, P. K.; Flannigan, D. J. Probing structural and electronic dynamics with ultrafast electron microscopy. *Chem. Mater.* **2015**, *27*, 3178−3192.

(19) Adhikari, A.; Eliason, J. K.; Sun, J.; Bose, R.; Flannigan, D. J.; Mohammed, O. F. Four-dimensional ultrafast electron microscopy: Insights into an emerging technique. *ACS Appl. Mater. Interfaces* **2017**, *9*, 3−16.

(20) Staykova, D. K.; Kuhs, W. F.; Salamatin, A. N.; Hansen, T. Formation of porous gas hydrates from ice powders: Diffraction experiments and multistage model. *J. Phys. Chem. B* **2003**, *107*, 10299−10311.

(21) Tung, Y.-T.; Chen, L.-J.; Chen, Y.-P.; Lin, S.-T. Growth of structure I carbon dioxide hydrate from molecular dynamics simulations. *J. Phys. Chem. C* **2011**, *115*, 7504−7515.

(22) Bauman, J. Kinetic Modelling of Hydrate Formation, Dissociation, and Reformation. Ph.D. Thesis, Dissertation for the Degree of Philosophiae Doctor (PhD), University of Bergen: Norway, 2015.
(23) Liu, C.; Zhang, Z.; Guo, G.-J. Effect of guests on the adsorption interaction between a hydrate cage and guests. *RSC Adv.* **2016**, *6*, 106443−106452.
(24) He, Z.; Linga, P.; Jiang, J. What are the key factors governing the nucleation of CO2 hydrate. *Phys. Chem. Chem. Phys.* **2017**, *19*, 15657−15661.
(25) Wilson, D. T.; Barnes, B. C.; Wu, D. T.; Sum, A. K. Molecular dynamics simulations of the formation of ethane clathrate hydrates *Fluid Phase Equilib.* 2016, *413*, 229 234 DOI: 10.1016/j.fluid.2015.12.001. Special Issue: Gas Hydrates and Semiclathrate Hydrates.
(26) Walsh, M. R.; Beckham, G. T.; Koh, C. A.; Sloan, E. D.; Wu, D. T.; Sum, A. K. Methane hydrate nucleation rates from molecular dynamics simulations: Effects of aqueous methane concentration, interfacial curvature, and system size. *J. Phys. Chem. C* **2011**, *115*, 21241−21248.
(27) Walsh, M. R.; Koh, C. A.; Sloan, E. D.; Sum, A. K.; Wu, D. T. Microsecond simulations of spontaneous methane hydrate nucleation and growth. *Science* **2009**, *326*, 1095−1098.
(28) Bolhuis, P. G.; Chandler, D.; Dellago, C.; Geissler, P. L. Transition path sampling: Throwing ropes over rough mountain passes, in the dark. *Annu. Rev. Phys. Chem.* **2002**, *53*, 291−318.
(29) Arjun; Berendsen, T. A.; Bolhuis, P. G. Unbiased atomistic insight in the competing nucleation mechanisms of methane hydrates. *Proc. Natl. Acad. Sci. U.S.A.* **2019**, *116*, 19305−19310.
(30) Costandy, J.; Michalis, V. K.; Tsimpanogiannis, I. N.; Stubos, A. K.; Economou, I. G. The role of intermolecular interactions in the prediction of the phase equilibria of carbon dioxide hydrates. *J. Chem. Phys.* **2015**, *143*, No. 094506.
(31) Abascal, J.; Sanz, E.; García Fernández, R.; Vega, C. A potential model for the study of ices and amorphous water: TIP4P/Ice. *J. Chem. Phys.* **2005**, *122*, No. 234511.
(32) others.; et al. OpenMM 7: Rapid development of high performance algorithms for molecular dynamics. *PLoS Comput. Biol.* **2017**, *13*, No. e1005659.
(33) Sivak, D. A.; Chodera, J. D.; Crooks, G. E. Time step rescaling recovers continuous-time dynamical properties for discrete-time Langevin integration of nonequilibrium systems. *J. Phys. Chem. B* **2014**, *118*, 6466−6474.
(34) Wilson, D. T.; Barnes, B. C.; Wu, D. T.; Sum, A. K. Molecular dynamics simulations of the formation of ethane clathrate hydrates. *Fluid Phase Equilib.* **2016**, *413*, 229−234.
(35) Chen, Y.; Chen, C.; Sum, A. K. Propane and Water: The Cooperativity of Unlikely Molecules to Form Clathrate Structures. *J. Phys. Chem. B* **2020**, *124*, 4661−4671.
(36) Swenson, D. W. H.; Prinz, J.-H.; Noe, F.; Chodera, J. D.; Bolhuis, P. G. OpenPathSampling: A Python framework for path sampling simulations. 1. Basics. *J. Chem. Theory Comput.* **2018**, *15*, 813−836.
(37) Trudu, F.; Donadio, D.; Parrinello, M. Freezing of a Lennard-Jones fluid: From nucleation to spinodal regime. *Phys. Rev. Lett.* **2006**, *97*, No. 105701.
(38) Zahn, D. Atomistic mechanism of NaCl nucleation from an aqueous solution. *Phys. Rev. Lett.* **2004**, *92*, No. 040801.
(39) Brotzakis, Z. F.; Bolhuis, P. G. A one-way shooting algorithm for transition path sampling of asymmetric barriers. *J. Chem. Phys.* **2016**, *145*, No. 164112.
(40) Barnes, B. C.; Beckham, G. T.; Wu, D. T.; Sum, A. K. Two-component order parameter for quantifying clathrate hydrate nucleation and growth. *J. Chem. Phys.* **2014**, *140*, No. 164506.
(41) Rodger, P.; Forester, T.; Smith, W. Simulations of the methane hydrate/methane gas interface near hydrate forming conditions conditions. *Fluid Phase Equilib.* **1996**, *116*, 326−332.
(42) McGibbon, R. T.; Beauchamp, K. A.; Harrigan, M. P.; Klein, C.; Swails, J. M.; Hernández, C. X.; Schwantes, C. R.; Wang, L.-P.; Lane, T. J.; Pande, V. S. MDTraj: a modern open library for the analysis of molecular dynamics trajectories. *Biophys. J.* **2015**, *109*, 1528−1532.
(43) Arjun, A.; Bolhuis, P. G. Rate Prediction for Homogeneous Nucleation of Methane Hydrate at Moderate Supersaturation Using Transition Interface Sampling. *J. Phys. Chem. B* **2020**, *124*, 8099−8109.
(44) Zhang, Z.; Walsh, M. R.; Guo, G.-J. Microcanonical molecular simulations of methane hydrate nucleation and growth: evidence that direct nucleation to sI hydrate is among the multiple nucleation pathways. *Phys. Chem. Chem. Phys.* **2015**, *17*, 8870−8876.
(45) Sarupria, S.; Debenedetti, P. G. Homogeneous nucleation of methane hydrate in microsecond molecular dynamics simulations. *J. Phys. Chem. Lett.* **2012**, *3*, 2942−2947.
(46) Weinan, E.; Ren, W.; Vanden-Eijnden, E. Transition pathways in complex systems: Reaction coordinates, isocommittor surfaces, and transition tubes. *Chem. Phys. Lett.* **2005**, *413*, 242−247.
(47) Ma, A.; Dinner, A. R. Automatic method for identifying reaction coordinates in complex systems. *J. Phys. Chem. B* **2005**, *109*, 6769−6779.
(48) Peters, B.; Trout, B. L. Obtaining reaction coordinates by likelihood maximization. *J. Chem. Phys.* **2006**, *125*, No. 054108.
(49) Jiménez-Ángeles, F.; Firoozabadi, A. Nucleation of methane hydrates at moderate subcooling by molecular dynamics simulations. *J. Phys. Chem. C* **2014**, *118*, 11310−11318.
(50) Maeda, N. Nucleation curve of carbon dioxide hydrate. *Energy Procedia* **2019**, *158*, 5928−5933.
(51) Radhakrishnan, R.; Trout, B. L. A new approach for studying nucleation phenomena using molecular simulations: application to CO 2 hydrate clathrates. *J. Chem. Phys.* **2002**, *117*, 1786−1796.
(52) Sloan, E., Jr.; Fleyfel, F. A molecular mechanism for gas hydrate nucleation from ice. *AIChE J.* **1991**, *37*, 1281−1292.
(53) Jacobson, L. C.; Hujo, W.; Molinero, V. Amorphous precursors in the nucleation of clathrate hydrates. *J. Am. Chem. Soc.* **2010**, *132*, 11806−11811.

https://dx.doi.org/10.1021/acs.jpcb.0c09915
J. Phys. Chem. B 2021, 125, 338−349